Biochimica et Biophysica Acta 1827 (2013) 438–445

Contents lists available at SciVerse ScienceDirect

Biochimica et Biophysica Acta

journal homepage: www.elsevier.com/locate/bbabio

Electronic structure of S_2 state of the oxygen-evolving complex of photosystem II studied by PELDOR

Mizue Asada [a], Hiroki Nagashima [a], Faisal Hammad Mekky Koua [b], Jian-Ren Shen [b], Asako Kawamori [c], Hiroyuki Mino [a,*]

[a] Division of Material Science (Physics), Graduate school of Science, Nagoya University, Furo-cho, Chikusa, Nagoya, 464-8602, Japan
[b] Graduate School of Natural Science and Technology/Faculty of Science; Okayama University, Okayama 700-8530, Japan
[c] AGAPE-Kabutoyama Institute of Medicine, Nishinomiya, Hyogo 662-0001, Japan

ARTICLE INFO

Article history:
Received 25 August 2012
Received in revised form 25 December 2012
Accepted 27 December 2012
Available online 8 January 2013

Keywords:
Photosystem II
Oxygen-evolving complex
Mn cluster
EPR
PELDOR

ABSTRACT

Photosynthetic water splitting is catalyzed by a Mn_4CaO_5 cluster in photosystem II, whose structure was recently determined at a resolution of 1.9 Å [Umena, Y. et al. 2011, *Nature*, 473:55–60]. To determine the electronic structure of the Mn_4CaO_5 cluster, pulsed electron–electron double resonance (PELDOR) measurements were performed for the tyrosine residue $Y_D^{\bullet}$ and S_2 state signals with non-oriented and oriented photosystem II (PS II) samples. Based on these measurements, the spin density distributions were calculated by comparing with the experimental results. The best fitting parameters were obtained with a model in which Mn1 has a large positive projection, Mn3 has a small positive projection, and Mn2 and Mn4 have negative projections (the numbering of Mn*i* ($i=1$–4) is based on the crystal structure at a 1.9 Å resolution), which yielded spin projections of 1.97, −1.20, 1.19 and −0.96 for Mn1–4 ions. The results show that the Mn1 ion, which is coordinated by H332, D342 and E189, has a valence of Mn(III) in the S_2 state. The sign of the exchange interactions J_{13} is positive, and the other signs are negative.

1. Introduction

Photosynthetic O_2 evolution is one of the most essential reactions for life on earth, because it produces O_2, protons and electrons from water. Protons and electrons are utilized to synthesize energy-rich compounds that are required for the synthesis of carbohydrates from carbon dioxide, whereas the O_2 maintains the oxygenic atmosphere that we enjoy today. The reaction is catalyzed by an oxygen-evolving complex (OEC) bound to a trans-membrane, multi-subunit protein complex designated photosystem (PS) II, located in the thylakoid membranes of cyanobacteria, algae, and green plants [1–3].

In addition to other protein subunits, PS II contains two reaction center proteins, D1/D2, whose structures are related by a pseudo C_2 symmetry. Light energy is absorbed by the reaction center chlorophylls P680 bound to the D1/D2 proteins, inducing charge separation and subsequent electron transfer reactions. The unpaired electron generated is subsequently transferred to bound plastoquinone molecules, Q_A/Q_B, in the stromal side of the membrane via pheophytin on the D1 protein. The paired hole on $P680^+$ is transferred to OEC in the lumenal side of PS II via a redox-active tyrosine residue, D1-Tyr161, which is designated Y_Z. Another tyrosine residue, D2-Tyr160, is located on the D2 protein in a position symmetric to that of Y_Z, giving rise to the stable tyrosine radical $Y_D^{\bullet}$.

In the water oxidation reaction, two water molecules are oxidized to yield an oxygen molecule through a cycle of five distinct redox states of OEC, which are designated as S_n ($n=0$–4). The S_1 state is the most stable state in the dark, and each S_n state advances to S_{n+1} by a single photon reaction in PS II. Upon successive photoreactions, the OEC advances to the highest oxidation state S_4 which is spontaneously converted to the lowest oxidation state S_0, concomitant with the release of an oxygen molecule [1–3]. The structure of OEC has been extensively studied with various techniques including visible, UV, and X-ray spectroscopic measurements, EPR and X-ray crystallography. In particular, previous X-ray crystallographic analysis has revealed the 3D structure of PS II at resolutions of 2.9–3.8 Å, which provided significant information on the overall structure of PS II as well as the locations of various subunits and cofactors including OEC containing 4 Mn atoms and 1 Ca atom [4–6]. However, the detailed structure of the Mn_4Ca cluster including the location of each metal ion and the oxo-bridges that connect them has not been resolved. Extended X-ray absorption fine structure (EXAFS) and polarized EXAFS

Abbreviations: EPR, electron paramagnetic resonance; PELDOR, pulsed electron–electron double resonance; ESE, electron spin echo; ESEEM, electron spin-echo envelope modulation; ENDOR, electron-nuclear double resonance; CW, continuous wave; MW, microwave; Mes, 2-Morpholinoethasulfonic acid; PS II, photosystem II; OEC, oxygen-evolving complex; Y_D, Tyr161 for higher plants (Tyr160 for cyanobacteria) of the D2 subunit in PS II; Y_Z, Tyr161 of the D1 subunit in PS II; ZFS, zero-field splitting

* Corresponding author. Tel./fax: +81 52 789 2882.
E-mail address: mino@bio.phys.nagoya-u.ac.jp (H. Mino).

0005-2728/$ – see front matter © 2013 Elsevier B.V. All rights reserved.
http://dx.doi.org/10.1016/j.bbabio.2012.12.011

have yielded various models for the structure of the Mn-cluster, and some of which have reached similar structures as that revealed by the crystallographic studies [7–12]. EXAFS studies have also provided information regarding the distances and orientations of Mn–Mn and Mn–Ca pairs [8,13–16]. In spite of these studies, ambiguities regarding the exact structure of the OEC still remained. This situation was changed dramatically by the success of recent structural analysis of PSII at a resolution of 1.9 Å, which revealed not only the locations of the individual metal ions but also the presence of the oxo-bridges connecting the metal ions, giving rise to a chemical formula of Mn_4CaO_5 for the OEC [17]. All of the amino acid residues ligating the metal cluster were identified, showing that each of the Mn ions is 6-coordinated and the Ca ion is 7-coordinated. The Mn_4CaO_5 cluster is organized in a distorted chair form with 3 Mn atoms (labeled Mn1–Mn3) and 1 Ca atom connected by 4 oxygen atoms to form a distorted cubic structure, and the 4th Mn (Mn4) and 5th oxygen (O4) connected outside of the cubane. The high-resolution structure also revealed that there are four water molecules ligated to the cluster, among which, two are ligated to Ca and the other two are ligated to Mn4. The amino acid residues ligated to Mn ions were D1-H332, D1-D342 and D1-E189 for Mn1, D1-D342, D1-A344 and CP43-E354 for Mn2, D1-E333 and CP43-E354 for Mn3 and D1-D170 and D1-E333 for Mn4 (Fig. 1).

During the S-state transition, the Mn_4CaO_5-cluster generates an EPR multiline signal in the S_2 state, which is the signpost for OEC in EPR studies. The multiline signal is centered at $g=2$ with an expansion over approximately 60 mT and is characterized by 19–21 hyperfine lines with a spacing of 8.5–9 mT between each pair of adjacent lines [18]. This signal has been ascribed to an overall $\boldsymbol{S_T}=1/2$ ground state arising from magnetically coupled 4 Mn ions. It has been proposed that the Mn cluster is a multinuclear complex in the S_2 state that includes a Mn(III)–Mn(IV) pair (reviewed in references [1–3]). Another multiline signal was found to arise in the S_0 state. This multiline signal is composed of at least 26 peaks that correspond to an $\boldsymbol{S}=1/2$ ground state in the presence of methanol [19,20]. ^{55}Mn-pulsed ENDOR results have revealed that the Mn cluster is a multinuclear complex in the S_2 state [19,20]. Kulik et al. suggested an oxidation state of 4Mn (III, IV, IV, IV) for the S_2 state based upon ^{55}Mn-pulsed ENDOR for the S_0 state [21]. ^{55}Mn-pulsed ENDOR has addressed the 4 sets of hyperfine constants (HFC) for the 4 Mn ions, where the largest set of HFC were assigned to the Mn(III) ion. In addition the HFC and spin projections of the Mn ions have been calculated. Because a unique solution of 6 exchange interactions J among the 4 Mn ions has not been experimentally determined, various models have been proposed. Peloquin et al. proposed a model with Mn ions coupled antiferro-magnetically [22]. Kulik et al. proposed a model with three Mn ions coupled antiferromagnetically in a triangular form, and one Mn ion isolated and coupled weakly to the three Mn ions antiferro-magnetically (Y-shape structure) [23]. Cox et al. proposed that the 4 Mn ions are connected with 6 exchange couplings based on a structure proposed by Siegbahn, which was obtained from theoretical studies using medium resolution X-ray structures and EXAFS data [24–27]. ESEEM studies suggested that the spin projection of the Mn ion coordinated to ^{14}N is Mn(III), where His332 has been proposed as a good ligand candidate based on a comparison with the results of H332E mutant studies [28,29].

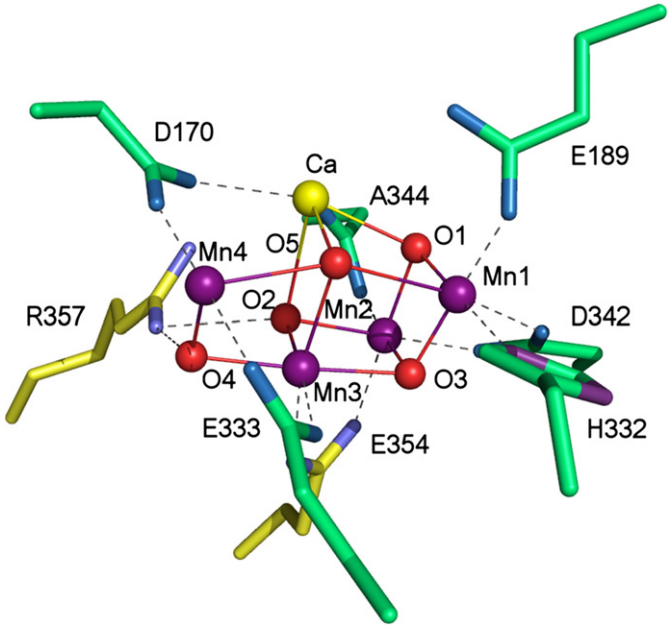

Fig. 1. The structure of the oxygen-evolving complex and its coordinating environment based on X-ray crystal spectroscopy (PDB: 3ARC).

Pulsed electron–electron double resonance (PELDOR) measurement is a well-established technique to determine the distances between electron spins [30]. PELDOR has been previously employed to measure the distance between $Y_D^{\bullet}$ and the S_2 Mn cluster [31]. The point dipole approximation showed that the distance between $Y_D^{\bullet}$ and the Mn cluster was 27 Å. However, the recent 1.9 Å PS II structure shows that the distances between the center of the aromatic ring of $Y_D^{\bullet}$ and each Mn ion are approximately 30 ± 2 Å. The inconsistency between the results may correspond to delocalization of the electron spins. In this work, we performed the PELDOR measurement and calculated the spin projections of each Mn ion in the S_2 state. Based on these results, the electronic structure of the Mn_4CaO_5-cluster in the S_2 state was determined.

2. Materials and methods

2.1. Sample preparation

Oxygen-evolving PS II core complexes were isolated from a thermophilic cyanobacterium *Thermosynechococcus vulcanus* as described previously [32,33]. The samples were suspended in a buffer containing 20 mM Mes (pH 6.0), 20 mM NaCl and 3 mM $CaCl_2$. Spinach PS II membranes were prepared as described in [34,35]. The samples were suspended in a buffer containing 400 mM sucrose, 20 mM NaCl and 20 mM Mes/NaOH (pH 6.5) and packed into EPR tubes. For the preparation of the oriented membrane samples, spinach PSII was dried on an OHP sheet under a humid nitrogen gas flow for 15 h at 4 °C. The sheets were cut into 2.5×25 mm^2 pieces and 6 pieces were collected, placed in an EPR tube, and frozen by rapidly placing the tube into liquid nitrogen (within 1 s). The bottom of the EPR tube contained glycerol to improve the heat conductivity in the EPR tubes. For the measurement of the S_1 state, the PS II samples were dark-adapted for 2–3 h after pre-illumination. The S_2 state of the samples was formed by illumination with white light for 5 min at 200 K.

2.2. EPR measurements

CW EPR measurements were performed by using a Bruker ESP-300E ESR spectrometer with a gas flow temperature control system (CF935, Oxford Instruments, Oxford, GB). ESE spectra were recorded on a Bruker pulsed EPR spectrometer ESP-380E by using an Oxford Instruments liquid helium cryostat. The pulsed ESE field swept spectra were measured by using a $\pi/2$–τ–π sequence with a time interval τ of 200 ns between the microwave (mw) pulses. A three-pulse PELDOR sequence was employed for the PELDOR measurements. The $\pi/2$–τ–π sequence with a time interval τ of 1000 ns between the mw pulses from the ESP380 source was used for observation. An mw synthesizer (HP83751A, Hewlett-Packard) was used as the mw source of 24 ns pumping pulse [31,36].

2.3. PELDOR simulations

The PELDOR signal amplitude $X(\tau')$ is a function of the time interval τ' between the 1st and 2nd pulses [31,36]:

$$X\left(\tau'\right) \propto 1-p\left[1-\cos\left(2\pi D\tau'\right)\right] \tag{1}$$

with

$$D=\frac{g_1 g_2 \beta^2}{hR^3}\left(1-3\cos^2\Theta\right) \tag{2}$$

where p is the fraction of the spin turned by the pumping pulse, D is the dipole interaction between the two spins, β is the Bohr magnetron and Θ is the angle between the external magnetic field $\boldsymbol{H}$ and the distance vector $\boldsymbol{R}$ between the two spins [31,36]. The parameters g_1 and g_2 are the g-factors for two electron spins, which were assumed to be 2.00 for $Y_D^{\bullet}$ and the S_2 multiline signal. The signal amplitude $I(\tau')$ is given by the integration over whole angles:

$$I\left(\tau'\right)=\int\int X\left(\tau'\right)\sin\theta d\theta d\varphi. \tag{3}$$

For precise PELDOR calculation of $Y_D^{\bullet}$ and the Mn cluster the spin density distribution must be included. The dipole interactions are expressed as follows:

$$D=\sum_{i,j}\rho_i\rho_j\frac{g_1 g_2 \beta^2}{hR_{ij}{}^3}\left(1-3\cos^2\Theta_{ij}\right) \tag{4}$$

where ρ_i is the spin density at the i-th ($i=1$–7) carbon/oxygen atom of the $Y_D^{\bullet}$ molecule and ρ_j is the spin projection at the j-th ($j=1$–4) Mn atom. The R_{ij} is the length between the i-th ($i=1$–7) carbon/oxygen atom of the $Y_D^{\bullet}$ and the j-th ($j=1$–4) Mn atom. The Θ_{ij} is the angle between the external magnetic field $\boldsymbol{H}$ and the distance vector $\boldsymbol{R_{ij}}$.

In the oriented PS II sample, the PELDOR intensities are given by:

$$I\left(\tau'\right)=\int\int X\left(\tau'\right)G(\theta-\theta_0)\sin\theta d\theta d\varphi \tag{5}$$

with

$$G(\theta-\theta_0)=\exp\left[-\frac{1}{2}\left(\frac{\theta-\theta_0}{\Delta}\right)^2\right] \tag{6}$$

where θ_0 is the angle between the membrane normal $\boldsymbol{n}$ and external field $\boldsymbol{H_0}$, and Δ is the distribution angle of the mosaic spread. $G(\theta-\theta_0)$ is the mosaic spread function which is assumed to be Gaussian. The z-axis was set to the membrane normal $\boldsymbol{n}$, along with the pseudo C_2 symmetric axis of PS II. The coordinates of $Y_D^{\bullet}$ and the Mn atoms were obtained from the 1.9 Å resolution X-ray structure (PDB: 3ARC). The spin densities on $Y_D^{\bullet}$ are shown in Fig. 2, which were obtained from the previous studies [37–41].

2.4. Spin projection

Spin Hamiltonian of the Mn cluster is written as follows:

$$H=\sum_i[\boldsymbol{H_0}\cdot\boldsymbol{g_i}\cdot\boldsymbol{S_i}+\boldsymbol{I_i}\cdot\boldsymbol{a_i}\cdot\boldsymbol{S_i}+\boldsymbol{S_i}\cdot\boldsymbol{D_i}\cdot\boldsymbol{S_i}]-\sum_{i<j}J_{ij}\boldsymbol{S_i}\cdot\boldsymbol{S_j} \tag{7}$$

where $\boldsymbol{S_i}$ and $\boldsymbol{I_i}$ are the operators of the electron spin and nuclear spin of the i-th Mn ion, respectively, $\boldsymbol{D_i}$ is the zero-field splitting (ZFS) tensor for the i-th Mn ion, $\boldsymbol{g_i}$ is the g-tensor and $\boldsymbol{a_i}$ is the hyperfine tensor of the i-th ion. J_{ij} is the exchange interaction between the i-th and j-th ion. When the ZFS effects are neglected, the spin Hamiltonian can be rewritten as:

$$\boldsymbol{H}=\mu_B\boldsymbol{H_0}\cdot\boldsymbol{g_i}\cdot\boldsymbol{S_T}+\sum_i\boldsymbol{I_i}\cdot\boldsymbol{A_i}\cdot\boldsymbol{S_T}-\sum_{i<j}J_{ij}\boldsymbol{S_i}\cdot\boldsymbol{S_j} \tag{8}$$

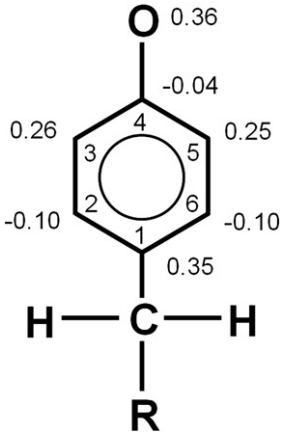

Fig. 2. Molecular structure and spin density distribution of the tyrosine neutral radical.

where $\boldsymbol{A_i}$ is the effective hyperfine tensor of the i-th ion. $\boldsymbol{S_T}$ is the total spin state with $\boldsymbol{S_T}=1/2$ for the S_2 state Mn cluster. The effective hyperfine tensor $\boldsymbol{A_i}$ and the local hyperfine tensor $\boldsymbol{a_i}$ are related by the following equation:

$$\boldsymbol{A_i}=\rho_i\boldsymbol{a_i} \tag{9}$$

where ρ_i is the spin density of the i-th ion. When the ZFS effects are neglected, the anisotropic portions of ρ_i can be neglected. The relationship between the isotropic portions of $\boldsymbol{A_i}$, $\boldsymbol{a_i}$ and ρ_i is given by:

$$\boldsymbol{A_{i,\mathrm{iso}}}=\rho_{i,\mathrm{iso}}\boldsymbol{a_{i,\mathrm{iso}}} \tag{10}$$

where $\rho_{i,iso}$ is identified as the spin projection and is defined by the value of the electron spin $\boldsymbol{S_i}$ as:

$$\rho_{i,\mathrm{iso}}=\frac{<S_iS_T>}{S_T(S_T+1)} \tag{11}$$

The values of the spin operator S_i for each Mn atom in the S_2 state have not been estimated experimentally. The effective hyperfine constants $A_{i,iso}$ in the S_2 state have been obtained by X- and Q-band ENDOR measurements, and the intrinsic hyperfine constants a_{iso} were estimated to be −165 to −225 MHz for Mn(III) and −187 to −253 MHz for Mn(IV), respectively [22,24]. The possible range of the spin projections are shown in Table 1.

3. Results

3.1. PELDOR experiments for the PS II solution samples

Fig. 3 shows the ESE field swept spectra in the (A) S_2 and (B) S_1 states of the PS II core complex samples, which were isolated from *T. vulcanus*. The signal with a 60 mT width centered at $g=2$ is the S_2 multiline, which arises from the $\boldsymbol{S}=1/2$ ground state of the Mn cluster. In the S_1 state, only the signal arising from Cyt *c550* was observed. The narrow signal centered at $g=2$ arises from $Y_D^{\bullet}$. Fig. 4 shows (A, B) PELDOR signals arising from the interaction between $Y_D^{\bullet}$ and the S_2 state of the Mn cluster in the (A) *T. vulcanus* and (B) spinach PS II samples and the simulated signals are also shown (C,D), which correspond to the case of the point dipole approximation with (C) 27 Å and (D) 30 Å. A three-pulse PELDOR sequence was employed, where the 1st and 3rd pulses were applied to the S_2 multiline signal for observation (filled array in Fig. 3) and the 2nd pulse was applied to $Y_D^{\bullet}$ for pumping (blank array in Fig. 3). The oscillations correspond to the magnetic dipole interaction between $Y_D^{\bullet}$ and the S_2 state Mn cluster. The oscillations in the spinach PS II has been previously reported [31]. The PELDOR oscillation in *T. vulcanus* PSII was very similar to that

Table 1
Spin projections of the Mn atoms calculated in previous studies.

Mn(III)	Mn(IV)	Mn(IV)	Mn(IV)	
1.70	1.27	−1.0	−0.99	Ref. [22]
1.73	1.10	−1.04	−0.79	Ref. [42]
1.73	1.12	−0.95	−0.90	Ref. [24]
1.39 to 1.89[a]	0.99 to 1.34[a]	−1.11 to −0.82[a]	−1.02 to −0.75[a]	Ref. [22,24]

[a] The fourth line shows the range of the spin projections, assuming A_{iso} of 165 to 225 MHz for a single Mn(III) and 187 to 253 MHz for a single Mn(IV).

observed for the spinach sample, which indicates that the PS II isolated from *T. vulcanus* and spinach have a similar structure in the lumenal side of the core complex. Some distortion in trace A might be ascribed to overlapping of the Chl^+ signals, which was about 15% overlapping on $Y_D^\bullet$ signal for *T. vulcanus* (data not shown). With the point dipole approximation, the distance between $Y_D^\bullet$ and the Mn cluster in the S_2 state was calculated to be 27 Å (trace C). However, the distances between $Y_D^\bullet$ and the Mn ions are 29.1, 31.9, 31.1 and 30.1 Å for the Mn*i* (*i* = 1–4) ions, respectively, in the high-resolution X-ray structure, assuming that the spin of $Y_D^\bullet$ is located at the center of its aromatic ring [7]. These distances are close to 30 Å, and the oscillation pattern using a 30 Å point dipole approximation is shown in trace D. This pattern is apparently different from the one shown in trace C, which was calculated from the observed PELDOR oscillation pattern. The inconsistency corresponds to the different contributions of the four spin projections of the Mn ions. Therefore, it is necessary to calculate an accurate PELDOR pattern using the spin density distribution on $Y_D^\bullet$, the Mn cluster and their coordinates.

3.2. PELDOR simulations including spin projections

The spin projections on the Mn atoms for the S_2 multiline signal have been calculated based on an EPR simulation, ENDOR, and DFT calculations [22,24,42]. These parameters are listed in Table 1. Peloquin et al. reported spin projections of 1.7, 1.27, −1 and −0.99 for the four Mn ions based on simulation of their ENDOR spectra [22]. Because a unique assignment of the spin projections to each of the four Mn ions could not be determined, several combinations of the projections and Mn ions were calculated by making some assumptions regarding the structural models. Assuming that two spin projections (i.e., −1 and −0.99) are equal to −1, twelve kinds of the combinations are possible. Fig. 5 shows the simulated PELDOR signals based on the possible combinations of the spin projections. The simulations were calculated by using Eqs. (4) and (5) as well as the resulting spin projections obtained by Peloquin et al. [22]. The numbering of the Mn ions is based on the structure reported by Umena et al. Maximum spin projections of 1.7, which is assumed to be on Mn(III), were assigned to (a1–a3) Mn1, (b1–3) Mn2, (c1–3) Mn3 and (d1–3) Mn4 [17]. The other positive spin projection (i.e., 1.27) was assigned to (a1–3) Mn2–4, (b1–3) Mn1, 3, 4, (c1–3) Mn1, 2, 4, and (d1–3) Mn1–3. The dotted lines show the positive peaks for the PELDOR oscillation in the experiments (Fig. 5). Some of the oscillation patterns, especially those for the spin projection combinations b2, c2 and d2 contrasted greatly with the experimental results. The PELDOR oscillations are similar to the experimental results when Mn1 has the largest spin projection of 1.7 (a1–3), or when Mn4 has the largest one and Mn1 has the other positive projection of 1.27 (d1). However, these simulated patterns (a1–3 and d1) are not completely consistent with the experimental results. Similarly the parameters obtained in other studies do not agree with the experimental results as well [23,24,42,43].

The spin projections were also estimated to be in the ranges of [1.39 to 1.89, 0.99 to 1.34, −1.11 to −0.82, −1.02 to −0.75] for the four Mn ions in the previous studies, assuming A_{iso} of 165–225 MHz for the single Mn(III) and 187–253 MHz for the Mn(IV) [22,24]. To determine if the simulation could yield a good fit with the experimental results, we calculated the PELDOR signals for the range of spin projections previously reported by increasing the margin by 10% (i.e., the positive values were calculated in the ranges of 1.2 to 2.0 and 0.9 to 1.5 and the negative values were calculated in the range of −1.2 to −0.65). For this calculation, the spin projections were varied by a resolution of 0.01 in the above ranges. The sum of the four projections was expected to be 1.00. We isolated the combinations of the Mn atom positions and the spin projections, which exhibit PELDOR oscillations with a negative peak at $\tau' = 200$ ns and positive peaks at $\tau' = 440$ and 800 ns, and they were clearly identical irrespective of combinations of the different spin projections (Fig. 6). A maximum limit of 5% was allowed for each value. The results show that three combinations were in good agreement with the experimental results. First, the largest

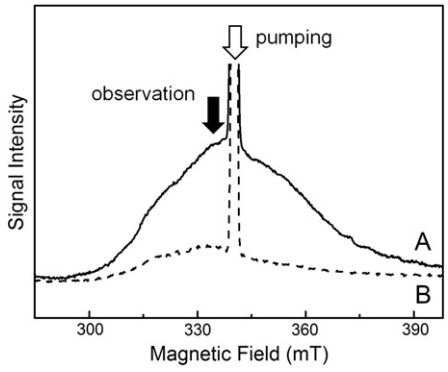

Fig. 3. Two-pulse ESE field swept spectra of *T. vulcanus* PS II. The spectra were obtained in the (A) S_2 and (B) S_1 states. Experimental conditions: microwave frequency, 9.60 GHz; pulse lengths, 16 ns for π/2 pulse s and 24 ns for π pulses; interval τ between the mw pulses, 200 ns; repetition time, 2 ms; temperature, 4 K. The arrows show the resonant magnetic fields for the observation (filled) and pumping (blank) microwave frequencies in the PELDOR measurement.

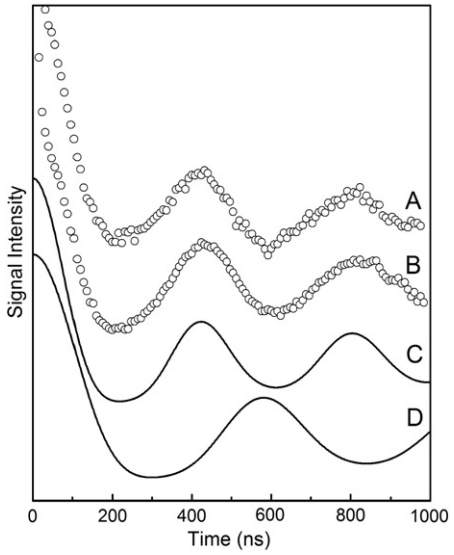

Fig. 4. (A, B) PELDOR spectra arising from the interaction between $Y_D^\bullet$ and the S_2 state of the Mn cluster in (A) *T. vulcanus* and (B) *spinach*, and (C,D) simulated spectra. S_2 multiline signals were used for observation and $Y_D^\bullet$ for pumping. Assuming a point dipole approximation between spin $\mathbf{S} = 1/2$ centers, the distances (C) 27 Å and (D) 30 Å were used for the simulation. Experimental conditions: observation microwave frequency, $\nu_1 = 9.61$ GHz; pumping microwave frequency, $\nu_2 = 9.73$ GHz; pulse lengths for ν_1, 16 ns and 24 ns; time interval between first and third pulses, $\tau = 1000$ ns; magnetic field, 348 mT; repetition time, 2 ms; temperature, 4 K.

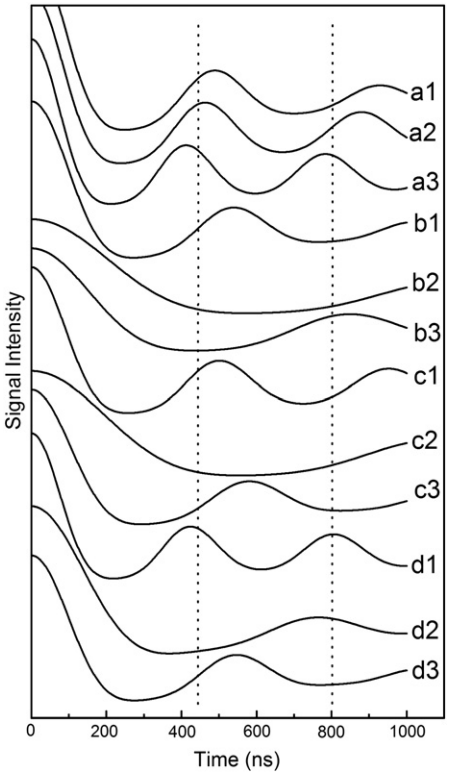

Fig. 5. Simulated PELDOR spectra arising from the interaction between $Y_D^{\bullet}$ and the Mn cluster in the S_2 state. The spin projections used for simulations were 1.7, 1.27, −1 and −1, which are based on a previous study [22]. The maximum spin projection is 1.7, assuming Mn(III), with (*a*1–*a*3) for Mn1, (*b*1–3) for Mn2, (*c*1–3) for Mn3 and (*d*1–3) for Mn4, respectively. The other positive spin production is 1.27 with (*a*1–3) for Mn2–4, (*b*1–3) for Mn1, 3, 4, (*c*1–3) for Mn1, 2, 4, and (*d*1–3) for Mn1–3. The dotted lines correspond to the peaks ($\tau' = 440$, 800 ns) in the experiment shown in Fig. 3A.

positive spin projection is located at Mn1 position and the other smaller positive one is located at Mn3, denoted [++, −, +, −] (Fig. 6, trace B). Second, the largest positive spin projection is located at Mn1 and the smaller positive one is located at Mn4, denoted [++, −, −, +] (Fig. 6, trace C). Finally, the largest positive projection spin is located at Mn4 and the smaller positive one is located at Mn1, denoted [+, −, −, ++] (Fig. 6, trace D). To distinguish these models, we measured the angular dependence of the PELDOR oscillations in the oriented PS II membranes.

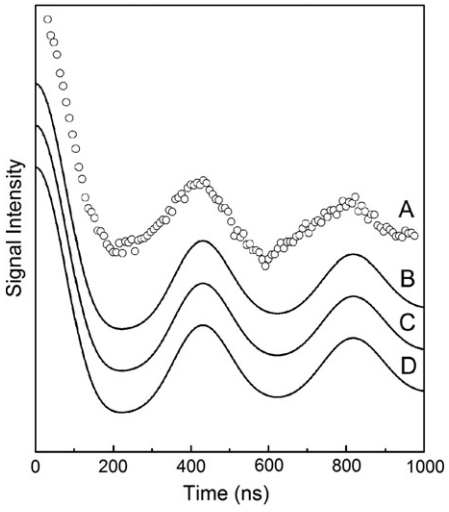

Fig. 6. (A) PELDOR spectra arising from the interaction between $Y_D^{\bullet}$ and the Mn cluster in the S_2 state of *T. vulcanus* and (B–D) simulated spectra. Trace (A) is the same as that shown in Fig. 3A. The spin projections used for the simulations for Mn1–4 were (B) 1.77, −1.07, 1.09 and −0.75, (C) 1.39, −0.75, −1.05 and 1.01 and (D) 1.17, −0.77, −0.77 and 1.39.

3.3. PELDOR experiment with the oriented PS II membranes

The mosaic spread angle for the oriented membranes was estimated by the g_Z peaks of the Cyt *b559* signal in the CW EPR. Fig. 7 shows that the signal intensities for the g_Z peak in the oriented PSII membranes reach a maximum when $\boldsymbol{H_0}$ was perpendicular to the membrane normal **n** ($\theta = 90°$) [44]. By fitting with the Gaussian function defined in Eq. (6), the mean square deviation Δ was estimated to be $17 \pm 0.5°$. Fig. 8 shows the PELDOR signals at (a) $\theta = 0°$ and (b) $\theta = 90°$ in the oriented PSII membranes. The PELDOR signal at $\theta = 0°$ appears to be in a monophasic oscillation because the angle between dipole vector **R** and external field $\boldsymbol{H_0}$ is uniquely determined within the distribution angles. The negative peak with $\tau' = 220$ ns at $\theta = 0°$ was shifted to $\tau' = 180$ ns at $\theta = 90°$, and the inflection with $\tau' = 300$ ns was observed at $\theta = 90°$. The other negative peak with $\tau' = 620$ ns at $\theta = 0°$ was shifted to $\tau' = 580$ ns at $\theta = 90°$. The positive peaks with $\tau' =$ 430 ns and 810 ns were the same at both $\theta = 0°$ and $\theta = 90°$. The simulations were performed with the manganese spin projection combinations fitted to the PELDOR measurements. The signals were fitted at the negative and positive peaks located at $\tau' = 220$, 430 and 810 ns with $\theta = 0°$ and at $\tau' = 180$, 430 and 810 ns with $\theta = 90°$. A maximum limit of 5% was allowed for each value. The best fit parameters were given in the model where Mn1 has the larger positive projection, Mn3 has the smaller positive projection and Mn2 and Mn4 have negative projections, denoted [++, −, +, −]. The possible range of the largest spin projection, which was assumed to belong to Mn(III), were 1.87–2.0 for [++, −, +, −].

The red line in Fig. 8 shows the best fit signal within this range of spin projections (i.e., 1.97, −1.2, 1.19 and −0.96 for Mn1–4, respectively). The broken and dotted lines are simulated signals for [++, −, −, +] and [+, −, −, ++] models, respectively. Fig. 9 shows the plots of the spin projections versus initial negative peak positions calculated. Panel A shows the larger positive spin projections. The gray area is the experimental range fitted within 5%. Circles show the spin projection of Mn1 in the model [++, −, +, −]. The model was fitted with the range of 1.87–2.00. Crosses and squares show the spin projections of Mn1 in the model [++, −, −, +] and Mn4 in the model [+, −, −, ++], respectively. The [++, −, −, +] and [+, −, −, ++] models were unable to be fitted within the 5% variation. The best fit parameters

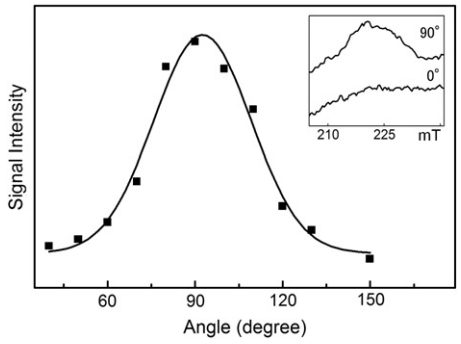

Fig. 7. Angular dependence of the CW EPR intensities of the g_Z peaks in Cyt *b*559 in the oriented spinach PS II sample. The angles are between the external field H_0 and membrane normal **n**. *Inset* shows the EPR spectra of the g_Z peaks at $\theta = 0°$ and 90°. The intensities were fitted to a Gaussian function $\Delta = 17°$ (see text). Experimental conditions: microwave frequency, 9.44 GHz; microwave power, 201 μW; temperature, 5 K. *Inset*: the CW EPR field swept spectra of the g_Z peaks in Cyt b559 at $\theta = 0°$ and 90°. Experimental conditions: microwave frequency, 9.44 GHz; microwave power, 201 μW; modulation amplitude, 8 mT.

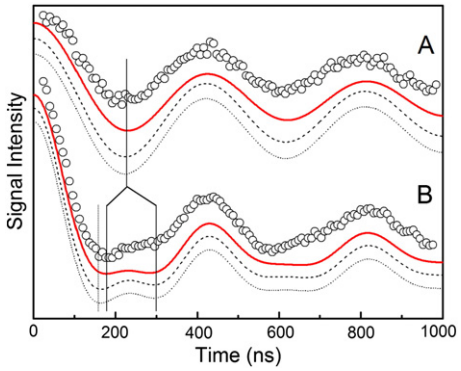

Fig. 8. (Circles) PELDOR spectra arising from the interaction between $Y_D^{\bullet}$ and the Mn cluster in the S_2 state of the orientated spinach PSII, and (bold, broken) the simulated spectra. The angles between the membrane normal **n** and external magnetic field $\boldsymbol{H_0}$ were (A) $\theta = 0°$and (B) 90°, respectively. The spin projections of the simulated spectra for Mn1–4 were (bold) 1.97, −1.2, 1.19 and −0.96, (broken) 1.4, −0.66, −0.65 and 0.91, and (dotted) 1.22, −0.75, −0.7 and 1.23. The vertical lines show the negative peak positions in the simulated spectra. Experimental conditions: observation microwave frequency, $\nu_1 = 9.61$ GHz; pumping microwave frequency, $\nu_2 = 9.73$ GHz; pulse lengths for ν_1, 16 ns and 24 ns; time interval between first and third pulses, $\tau =$ 1000 ns; magnetic field, 348 mT; repetition time, 2 ms; temperature, 4 K.

were 1.38–1.41 for [++, −, −, +] and 1.21–1.5 for [+, −, −, ++]. Panel B shows the smaller positive spin projections. Panels C and D show the negative spin projections, where (C) Mn2 in the all models is in one negative spin projection and (D) Mn4 in the model [++, −, +, −] or Mn3 in the model [++, −, −, +] and [+, −, −, ++] are in the other negative spin projection. The possible ranges of the spin projection sets for these models are listed in Table 2. The broken and dotted lines in Fig. 8 are simulated signals for the [++, −, −, +] and [+, −, −, ++] models, respectively.

4. Discussion

Several EPR studies have been performed to investigate the structure of the OEC, and these studies have aided in the elucidation of the structure and function of OEC. ^{55}Mn-pulsed ENDOR studies have revealed the hyperfine couplings of four manganese ions in the S_0 and S_2 states, and concluded that the oxidation states of Mn_4 are (III, III, III, IV) for the S_0 state and (III, IV, IV, IV) for the S_2 state [22,23]. However, the couplings between the manganese ions and the valences of each of the four manganese ions were not directly correlated with the structure. It was difficult to understand the relationship between the molecular structure obtained by X-ray crystallography and the magnetic interactions obtained by EPR. Based on the ^{55}Mn-pulsed ENDOR results, the most favorable model is a '3 + 1' Mn tetramer. In this model, the four manganese ions are arranged in a Y-shape, in which the triangle unit, which is denoted Mn_{BCD}, is tightly coupled, and a fourth Mn, which is denoted Mn_A, is coupled to one Mn_B in the triangle unit. The nomenclatures of Mn_{A-D} corresponded to that of Mn1–Mn4 in the 1.9A structure in the following way: $Mn_A = Mn4$, $Mn_B = Mn3$, $Mn_C = Mn2$, $Mn_D = Mn1$. In this model, the position of Mn(III) was ambiguous. Kulik et al. assigned Mn(III) to Mn_A or Mn_C. Based on the comparison of the S_0 and S_2 ENDOR results, Mn(III) was assigned to Mn_A [21]. In contrast, Charlot et al. have assigned Mn(III) to the trimer side, denoted as Mn_C and Mn_D [42]. These models excluded the possibility that Mn(III) is located at the center of the Y-shaped structure, denoted Mn_B. Based on quantum chemical calculations and EXAFS spectroscopy, a model (Siegbahn model) was proposed in which four manganese ions were connected with 6 exchange couplings J [24,45,46]. The couplings of Mn_A–Mn_B and Mn_C–Mn_D were assigned to be antiferro-magnetic [24,45,46], where the Mn_C and Mn_D are arbitrary from an electronic perspective [24]. The model was consistent with the Kulik model when Mn(III) was assigned to Mn_C. In these models, the location of the Mn(III) has been assigned to the largest hyperfine couplings of the four manganese ions [21,22].

To clarify these ambiguities, we measured the PELDOR signals between $Y_D^{\bullet}$ and the S_2 multiline signals in the oriented and non-oriented PS II samples, to determine the spin projections of the Mn ions with coordinates taken from the 1.9 Å structure. The obtained results show that (1) the Mn ion, denoted as Mn1, is Mn(III); (2) the most likely spin projections of the Mn ions is obtained with the [++, −, +, −] model, where the projections were 1.97, −1.19, 1.17 and −0.95 for each Mni (i = 1–4), respectively. The results are in good agreement with the ^{14}N ESEEM results, where the spin projection of the Mn(III) ion estimated from the ^{14}N parameters was approximately 2 and located on the His332 side [28,29]. The result (2) enables us to determine the

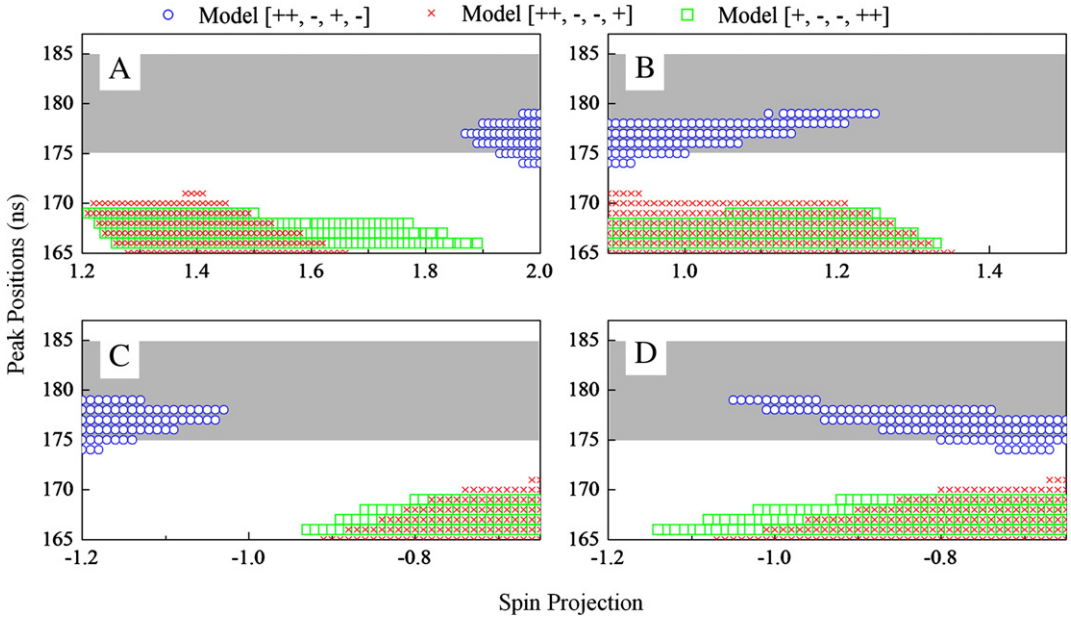

Fig. 9. The calculation for spin projections and the initial negative peak positions for PELDOR oscillation. Panels A and B show (A) the larger and (B) smaller positive spin projections, respectively. Panels C and D show the negative spin projections, where (C) Mn2 in the all models is in one negative spin projection and (D) Mn4 in the model [++, −, +, −] or Mn3 in the model [++, −, −, +] and [+, −, −, ++] are in the other negative spin projection. The circles, triangles and crosses show the model [++, −, +, −], model [++, −, −, +] and model [+, −, −, ++], respectively. The gray area shows the experimental fitted range within 5%.

Table 2
Range of the spin projections obtained from fitting.

Mn1	Mn2	Mn3	Mn4	Combinations	Error range	
1.68 to 2.00	−1.20 to −0.65	0.90 to 1.50	−1.20 to −0.65	[++, −, +, −]	<5%	Non-oriented PS II
1.20 to 1.71	−1.09 to −0.65	−1.20 to −0.65	0.90 to 1.50	[++, −, −, +]	<5%	
0.90 to 1.50	−1.19 to −0.65	−1.20 to −0.65	1.20 to 2.00	[+, −, −, ++]	<5%	
1.87 to 2.00	−1.20 to −1.03	0.90 to 1.25	−1.05 to −0.65	[++, −, +, −]	<5%	Oriented PS II
1.38 to 1.41	−0.66 to −0.65	−0.67 to −0.65	0.90 to 0.94	[++, −, −, +]	>5%	
1.06 to 1.25	−0.65 to −0.80	−0.92 to −0.65	1.21 to 1.50	[+, −, −, ++]	>5%	

The error range was within 5% for the models in the non-oriented PS II and the [++, −, +, −] model in the oriented PS II, and over 5% for [++, −, −, +] and [+, −, −, ++] models in the oriented PS II.

signs of the exchange couplings *J*, which are shown in Fig. 10. The antiferromagnetic couplings were assigned to Mn1–Mn2 and Mn3–Mn4. Based on the 1.9 Å crystal structure, the distance between the Mn atom is 2.8–2.9 Å for Mn1–Mn2 and Mn2–Mn3, which are the closest Mn pairs in the OEC. Therefore, it may be natural that the closest Mn pairs involve antiferromagnetic couplings. It is important to note that our results directly assigned the spin projections to the location of the manganese ions in the OEC by the inclusion of the coordinates in the calculation. Although our results were independently obtained, they are consistent with previous models assuming that the Mn_C(Mn2) and Mn_D(Mn1) are arbitrary from an electronic perspective [21,24,46].

In this paper, the [++, −, +, −] model fit to the PELDOR results better than the models [++, −, −, +] and [+, −, −, ++]. Although our calculations were based on the assumption that the largest spin projection arises from Mn(III) in the range of 1.2–2.0, the [++, −, −, +] and [+, −, −, ++] models gave a spin projection of less than 1.5 for Mn(III) in the oriented sample. These results are inconsistent with the ^{14}N ESEEM results [28,29].

Although several model structures have been proposed, the exact structure of the S_2 state is still unknown [46,47]. Ames et al. have proposed that there is no bonding of Mn1–O in the S_2 states, which results in a structural change of approximately 0.3 Å for Mn4 [46]. We checked the influence on the PELDOR signal by changing the coordinates of the Mn4 atom by 0.3 Å. Our trial simulations show that the oscillation pattern of PELDOR would change by less than 5% for the [++, −, +, −] and [++, −, −, +] models, and less than 10% for the [+, −, −, ++] model. However, in these cases the best fitted model was still [++, −, +, −]. These results indicate that the small change of the position of Mn4 causes little influence on the PELDOR oscillation patterns. Therefore, it seems that structural modification is not the critical reason for the inconsistency in these models. Another possibility may exist, because our present calculation does not include the anisotropic effects of the projection factors. The DFT calculations support the [++, −, −, +] model [24,46], which is consistent with the EXAFS and ^{55}Mn ENDOR results [10,22,23,48]. Based on the DFT calculation, large anisotropic spin projections on each Mn atom are proposed [24], which might influence the PELDOR interpretation of the PELDOR results. To clarify this, the anisotropic effects of the spin projections on the Mn ions should be considered. If it is possible to fit the PELDOR results to the model [++, −, −, +] by using the DFT parameters, it would provide more detailed information on the S_2 state. Further analysis to clarify the anisotropic effects is in progress.

5. Conclusion

By using the PELDOR method, the spin projections in the S_2 state of the Mn_4CaO_5 cluster were directly estimated from the 1.9 Å crystal structure. The best fit parameters for the PELDOR experiments were obtained in the model in which Mn1 and Mn3 have positive signs, and the projections were determined to be 1.97, −1.19, 1.17 and −0.95 for Mn*i* (i=1–4), respectively. The Mn1 ion in the S_2 state of the Mn_4CaO_5 cluster, was assigned to be Mn(III). The antiferromagnetic couplings were assigned to Mn1–Mn2 and Mn3–Mn4, and the ferromagnetic coupling was assigned to Mn1–Mn3.

Acknowledgement

This work was supported by a MEXT/JSPS Grant-in-Aid for Exploratory Research No. 22684051 and by a grant from the Kurata Foundation to H. M., and by a MEXT/JSPS Grant-in-Aid for Specially Promoted Research No. 24000018 to J-R. S.

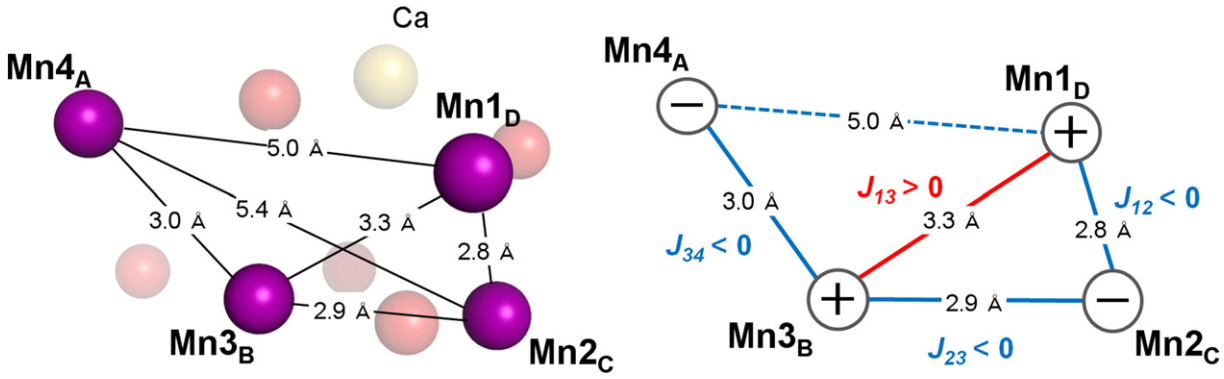

Fig. 10. (Left) Molecular structure and the distances between the pairs of Mn atoms based on the 1.9 Å structure [17]. (Right) Exchange coupling model for the S_2-state of the Mn cluster. Only exchange couplings with close distances near 3 Å are shown.

References

[1] J.P. McEvoy, G.W. Brudvig, Water-splitting chemistry of photosystem II, Chem. Rev. 106 (2006) 4455–4483.
[2] N. Nelson, C.F. Yocum, Structure and function of photosystems I and II, Annu. Rev. Plant Biol. 57 (2006) 521–565.
[3] J. Messinger, G. Renger, Photosynthetic water-splitting, in: G. Renger (Ed.), Primary Processes of Photosynthesis, Part II: Basic Principles and Apparatus, Royal Society of Chemistry, Cambridge, 2008, pp. 291–349.
[4] K.N. Ferreira, T.M. Iverson, K. Maghlaoui, J. Barber, S. Iwata, Architecture of the photosynthetic oxygen-evolving center, Science 303 (2004) 1831–1838.
[5] B. Loll, J. Kern, W. Saenger, A. Zouni, J. Biesiadka, Towards complete cofactor arrangement in the 3.0 Å resolution structure of photosystem II, Nature 438 (2005) 1040–1044.
[6] A. Guskov, J. Kern, A. Gabdulkhakov, M. Broser, A. Zouni, W. Saenger, Cyanobacterial photosystem II at 2.9 Å resolution and the role of quinones, lipids, channels and chloride, Nat. Struct. Mol. Biol. 16 (2009) 334–342.
[7] V.K. Yachandra, K. Sauer, M.P. Klein, Manganese cluster in photosynthesis: where plants oxidize water to dioxygen, Chem. Rev. 96 (1996) 2927–2950.
[8] J. Yano, Y. Pushkar, P. Glatzel, A. Lewis, K. Sauer, J. Messinger, U. Bergmann, V. Yachandra, High-resolution Mn EXAFS of the oxygen-evolving complex in photosystem II: structural implications for the Mn_4Ca cluster, J. Am. Chem. Soc. 127 (2005) 14974–14975.
[9] J.H. Robblee, J. Messinger, R.M. Cinco, K.L. McFarlane, C. Fernandez, S.A. Pizarro, K. Sauer, V.K. Yachandra, The Mn cluster in the S_0 state of the oxygen-evolving complex of photosystem II studied by EXAFS spectroscopy: are there three di-μ-oxo-bridged Mn_2 moieties in the tetranuclear Mn complex? J. Am. Chem. Soc. 124 (2002) 7459–7471.
[10] J. Yano, J. Kern, K. Sauer, M.J. Latimer, Y. Pushkar, J. Biesiadka, B. Loll, W. Saenger, J. Messinger, A. Zouni, V.K. Yachandra, Where water is oxidized to dioxygen: structure of the photosynthetic Mn_4Ca cluster, Science 314 (2006) 821–825.
[11] R.M. Cinco, J.H. Robblee, J. Messinger, C. Fernandez, K.L.M. Holman, K. Sauer, V.K. Yachandra, Orientation of calcium in the Mn_4Ca cluster of the oxygen-evolving complex determined using polarized strontium EXAFS of photosystem II membranes, Biochemistry 43 (2004) 13271–13282.
[12] Y. Pushkar, J. Yano, P. Glatzel, J. Messinger, A. Lewis, K. Sauer, U. Bergmann, V. Yachandra, Structure and orientation of the Mn_4Ca cluster in plant photosystem II membranes studied by polarized range-extended X-ray absorption spectroscopy, J. Biol. Chem. 282 (2007) 7198–7208.
[13] J. Yano, V.K. Yachandra, Oxidation state changes of the Mn_4Ca cluster in photosystem II, Photosynth. Res. 92 (2007) 289–303.
[14] J. Yano, V.K. Yachandra, Where water is oxidized to dioxygen: structure of the photosynthetic Mn_4Ca cluster from X-ray spectroscopy, Inorg. Chem. 47 (2008) 1711–1726.
[15] K. Sauer, J. Yano, V.K. Yachandra, X-ray spectroscopy of the Mn_4Ca cluster in the water-oxidation complex of Photosystem II, Photosynth. Res. 85 (2005) 73–86.
[16] K. Sauer, J. Yano, V.K. Yachandra, X-ray spectroscopy of the photosynthetic oxygen-evolving complex, Coord. Chem. Rev. 252 (2008) 318–335.
[17] Y. Umena, K. Kawakami, J.R. Shen, N. Kamiya, Crystal structure of oxygen-evolving photosystem II at a resolution of 1.9 Å, Nature 473 (2011) 55–60.
[18] G.C. Dismukes, Y. Siderer, Intermediates of a polynuclear manganese center involved in photosynthetic oxidation of water, Proc. Natl. Acad. Sci. 78 (1981) 274–278.
[19] J. Messinger, J.H. Robblee, W.O. Yu, K. Sauer, V.K. Yachandra, M.P. Klein, The S_0 state of the oxygen-evolving complex in photosystem II is paramagnetic: detection of EPR multiline signal, J. Am. Chem. Soc. 119 (1997) 11349–11350.
[20] P. Geijer, S. Peterson, K.A. Åhrling, Z. Deak, S. Styring, Comparative studies of the S_0 and S_2 multiline electron paramagnetic resonance signals from the manganese cluster in photosystem II, Biochim. Biophys. Acta 1503 (2001) 83–95.
[21] L.V. Kulik, B. Epel, W. Lubitz, J. Messinger, Electronic structure of the Mn_4OxCa cluster in the S_0 and S_2 states of the oxygen-evolving complex of photosystem II based on pulse ^{55}Mn-ENDOR and EPR spectroscopy, J. Am. Chem. Soc. 129 (2007) 13421–13435.
[22] J.M. Peloquin, K.A. Campbell, D.W. Randall, M.A. Evanchik, V.L. Pecoraro, W.H. Armstrong, R.D. Britt, ^{55}Mn ENDOR of the S_2-state multiline EPR signal of photosystem II: implications on the structure of the tetranuclear Mn cluster, J. Am. Chem. Soc. 122 (2000) 10926–10942.
[23] L.V. Kulik, B. Epel, W. Lubitz, J. Messinger, ^{55}Mn pulse ENDOR at 34 GHz of the S_0 and S_2 states of the oxygen-evolving complex in photosystem II, J. Am. Chem. Soc. 127 (2005) 2392–2393.
[24] N. Cox, L. Rapatskiy, J.H. Su, D.A. Pantazis, M. Sugiura, L. Kulik, P. Dorlet, A.W. Rutherford, F. Neese, A. Boussac, W. Lubitz, J. Messinger, Effect of Ca^{2+}/Sr^{2+} substitution on the electronic structure of the oxygen-evolving complex of photosystem II: a combined multifrequency EPR, ^{55}Mn-ENDOR, and DFT study of the S_2 state, J. Am. Chem. Soc. 133 (2011) 3635–3648.
[25] P.E.M. Siegbahn, Structures and energetics for O_2 formation in photosystem II, Acc. Chem. Res. 42 (2009) 1871–1880.
[26] P.E.M. Siegbahn, A structure-consistent mechanism for dioxygen formation in photosystem II, Chem. Eur. J. 14 (2008) 8290–8302.
[27] P.E.M. Siegbahn, An energetic comparison of different models for the oxygen evolving complex of photosystem II, J. Am. Chem. Soc. 131 (2009) 18238–18239.
[28] T.A. Stich, G.J. Yeagle, R.J. Service, R.J. Debus, R.D. Britt, Ligation of D1-His332 and D1-Asp170 to the manganese cluster of photosystem II from *Synechocystis* assessed by multifrequency pulse EPR spectroscopy, Biochemistry 50 (2011) 7390–7404.
[29] G.J. Yeagle, M.L. Gilchrist, R.M. McCarrick, R.D. Britt, Multifrequency pulsed electron paramagnetic resonance study of the S_2 state of the photosystem II manganese cluster, Inorg. Chem. 47 (2008) 1803–1814.
[30] J.E. Banham, C.M. Baker, S. Ceola, I.J. Day, G.H. Grant, E.J.J. Groenen, C.T. Rodgers, G. Jeschke, C.R. Timmel, Distance measurements in the borderline region of applicability of CW EPR and DEER: a model study on a homologous series of spin-labelled peptides, J. Magn. Reson. 191 (2008) 202–218.
[31] H. Hara, A. Kawamori, A.V. Astashkin, T. Ono, The distances from tyrosine D to redox-active components on the donor side of photosystem II determined by pulsed electron–electron double resonance, Biochim. Biophys. Acta 1276 (1996) 140–146.
[32] J.R. Shen, Y. Inoue, Binding and functional-properties of two new extrinsic components, cytochrome-C-550 and a 12-kDa protein, in cyanobacterial photosystem II, Biochemistry-Us 32 (1993) 1825–1832.
[33] J.R. Shen, N. Kamiya, Crystallization and the crystal properties of the oxygen-evolving photosystem II from *Synechococcus vulcanus*, Biochemistry-Us 39 (2000) 14739–14744.
[34] D.A. Berthold, G.T. Babcock, C.F. Yocum, A highly resolved oxygen-evolving photosystem-ii preparation from spinach thylakoid membranes — EPR and electron-transport properties, FEBS Lett. 134 (1981) 231–234.
[35] T. Ono, Y. Inoue, Effects of removal and reconstitution of the extrinsic 33, 24 and 16 kDa proteins on flash oxygen yield in photosystem-II particles, Biochim. Biophys. Acta 850 (1986) 380–389.
[36] Y. Asada, R. Mutoh, M. Ishiura, H. Mino, Nonselective excitation of pulsed ELDOR using multi-frequency microwaves, J. Magn. Reson. 213 (2011) 200–205.
[37] C.W. Hoganson, G.T. Babcock, Protein tyrosyl radical interactions in photosystem-II studied by electron-spin-resonance and electron nuclear double-resonance spectroscopy — comparison with ribonucleotide reductase and in vitro tyrosine, Biochemistry 31 (1992) 11874–11880.
[38] H. Nagai, Y. Fukushima, K. Okajima, M. Ikeuchi, H. Mino, Formation of interacting spins on flavosemiquinone and tyrosine radical in photoreaction of a blue light sensor BLUF protein TePixD, Biochemistry 47 (2008) 12574–12582.
[39] H. Mino, A.V. Astashkin, A. Kawamori, An EPR and pulsed ENDOR study of the structure of tyrosine $Z^{\bullet}$ in Tris-treated photosystem II, Spectrochim. Acta A 53 (1997) 1465–1483.
[40] W. Hofbauer, A. Zouni, R. Bittl, J. Kern, P. Orth, F. Lendzian, P. Fromme, H.T. Witt, W. Lubitz, Photosystem II single crystals studied by EPR spectroscopy at 94 GHz: the tyrosine radical $Y_D^{\bullet}$, Proc. Natl. Acad. Sci. U. S. A. 98 (2001) 6623–6628.
[41] S. Kessen, C. Teutloff, J. Kern, A. Zouni, R. Bittl, High-field ^{2}H-Mims-ENDOR spectroscopy on PSII single crystals: hydrogen bonding of $Y_D^{\bullet}$, Chemphyschem 11 (2010) 1275–1282.
[42] M.F. Charlot, A. Boussac, G. Blondin, Towards a spin coupling model for the Mn_4 cluster in photosystem II, Biochim. Biophys. Acta 1708 (2005) 120–132.
[43] M. Zheng, G.C. Dismukes, Orbital configuration of the valence electrons, ligand field symmetry, and manganese oxidation states of the photosynthetic water oxidizing complex: analysis of the S_2 state multiline EPR signals, Inorg. Chem. 35 (1996) 3307–3319.
[44] K. Hasegawa, M. Kusunoki, Y. Inoue, T.A. Ono, Simulation of S_2 state multiline EPR signal in oriented photosystem II membranes: structural implications for the manganese cluster in an oxygen-evolving complex, Biochemistry 37 (1998) 9457–9465.
[45] D.A. Pantazis, M. Orio, T. Petrenko, S. Zein, W. Lubitz, J. Messinger, F. Neese, Structure of the oxygen-evolving complex of photosystem II: information on the S_2 state through quantum chemical calculation of its magnetic properties, Phys. Chem. Chem. Phys. 11 (2009) 6788–6798.
[46] W. Ames, D.A. Pantazis, V. Krewald, N. Cox, J. Messinger, W. Lubitz, F. Neese, Theoretical evaluation of structural models of the S_2 state in the oxygen evolving complex of photosystem II: protonation states and magnetic interactions, J. Am. Chem. Soc. 133 (2011) 19743–19757.
[47] S. Schinzel, J. Schraut, A.V. Arbuznikov, P.E.M. Siegbahn, M. Kaupp, Density functional calculations of ^{55}Mn, ^{14}N and ^{13}C electron paramagnetic resonance parameters support an energetically feasible model system for the S_2 state of the oxygen-evolving complex of photosystem II, Chem. Eur. J. 16 (2010) 10424–10438.
[48] L. Rapatskiy, N. Cox, A. Savitsky, W.M. Ames, J. Sander, M.M. Nowaczyk, M. Rögner, A. Boussac, F. Neese, J. Messinger, W. Lubitz, Detection of the water-binding sites of the oxygen-evolving complex of photosystem II 'using W-band ^{17}O electron–electron double resonance-detected NMR spectroscopy, J. Am. Chem. Soc. 134 (2012) 16619–16634.